

Journal Pre-proof



Concentration-gradient driven atom diffusion to synthesize high-loaded and sub-5 nm PtCo intermetallic compound for fuel cells

Qingqing Cheng, Tao Wang, Yihe Chen, Yongyu Pan, Yubin Chen, Bo Yang, Hui Yang

PII: S2667-1417(25)00083-7

DOI: <https://doi.org/10.1016/j.esci.2025.100453>

Reference: ESCI 100453

To appear in: eScience

Received Date: 8 April 2025

Revised Date: 7 June 2025

Accepted Date: 9 July 2025

Please cite this article as: Q. Cheng, T. Wang, Y. Chen, Y. Pan, Y. Chen, B. Yang, H. Yang, Concentration-gradient driven atom diffusion to synthesize high-loaded and sub-5 nm PtCo intermetallic compound for fuel cells, [eScience](https://doi.org/10.1016/j.esci.2025.100453), <https://doi.org/10.1016/j.esci.2025.100453>.

This is a PDF file of an article that has undergone enhancements after acceptance, such as the addition of a cover page and metadata, and formatting for readability, but it is not yet the definitive version of record. This version will undergo additional copyediting, typesetting and review before it is published in its final form, but we are providing this version to give early visibility of the article. Please note that, during the production process, errors may be discovered which could affect the content, and all legal disclaimers that apply to the journal pertain.

© 2025 The Authors. Publishing services by Elsevier B.V. on behalf of Nankai University and KeAi.

1 **Concentration-gradient driven atom diffusion to synthesize
2 high-loaded and sub-5 nm PtCo intermetallic compound for
3 fuel cells**

4
5 Qingqing Cheng ^{a,*}, Tao Wang ^b, Yihe Chen ^b, Yongyu Pan ^a, Yubin Chen ^a, Bo Yang ^b,
6 Hui Yang ^{a,c,*}

7 ^a *Shanghai Advanced Research Institute, Chinese Academy of Science, Shanghai
201210, China*

8 ^b *School of Physical Science and Technology, ShanghaiTech University, Shanghai
201210, China*

9 ^c *CAHM Technology (Foshan) Co., Ltd, Foshan 528216, China*

10

11 *Corresponding authors.

12 E-mails: chengqq@sari.ac.cn (Qingqing Cheng), yangh@sari.ac.cn (Hui Yang).

13

14

15

16

17

Abstract

18 The synthesis of Pt intermetallic compounds (IMCs) typically necessitates high-
19 temperature annealing to overcome the atom-diffusion kinetic barrier, which inevitably
20 results in considerable nanoparticle sintering, especially for the high-loaded catalyst,
21 thus leading to diminished performance in proton exchange membrane fuel cells. We
22 propose a concentration-gradient-driven atom diffusion strategy to synthesize Pt
23 intermetallic compounds (IMCs), overcoming the atom-diffusion kinetic barrier under
24 relatively low temperature. This method efficiently transforms high-loaded Pt seeds/C
25 into sub-5 nm L₁₀-PtCo-IMC/C (44.3 wt.%) catalyst. Advanced characterizations and
26 molecular dynamic simulations reveal that locally concentrated Co precursors
27 accelerate atom diffusion and enhance nanoparticle anti-sintering ability. Temperature-
28 dependent analyses further elucidate the structural transformation mechanism by
29 tracking crystal structure and nanoparticle size evolution. Membrane electrode
30 assembly (MEA) integrated with the optimized PtCo-IMC/C at a low Pt usage (0.1 mg
31 cm⁻²) delivers a maximum power density of approximately 1.15 W cm⁻² and excellent

1 stability (a 26-mV loss at 0.8 A cm^{-2}) after 30000 cycles of accelerated stress testing
2 under H₂-air conditions. This scalable synthesis pathway (20 g per batch) holds great
3 promise for advancing high-loaded fuel cell electrocatalysts.

4 *Keywords:* High-loaded catalyst, Intermetallic compounds; Concentration-gradient;
5 Oxygen reduction reaction; Proton exchange membrane fuel cells

6

7

8

9 1. Introduction

10 Proton exchange membrane fuel cells (PEMFCs) are widely recognized as a promising
11 clean energy alternative to traditional energy sources due to their high energy
12 conversion efficiency, environmental friendliness, and operation under low-
13 temperature conditions [1]. However, the large-scale commercialization of PEMFCs is
14 significantly hindered by the high demand for Pt-based catalysts [2–4]. Among these,
15 cathodic catalysts play a crucial role in determining the overall performance and
16 stability of PEMFCs, largely due to the inherently sluggish kinetics of the oxygen
17 reduction reaction (ORR). Although carbon-supported platinum (Pt/C) is currently the
18 benchmark ORR electrocatalyst, its suboptimal activity and durability remain
19 significant challenges for its practical application in PEMFC vehicles [5–7]. Carbon
20 supported Pt intermetallic compounds (PtM-IMCs/C, where M = Fe, Co, Ni, etc.) [8,9]
21 present distinct advantages, such as well-defined atomic arrangements and unique
22 electronic structures, over their disordered alloy counterparts [10,11], positioning them
23 as promising candidates for efficient ORR electrocatalysts [12–14]. However, the
24 formation of IMC structures typically necessitates high temperature [15] and prolonged
25 annealing times to overcome the energy barrier associated with atom diffusion during

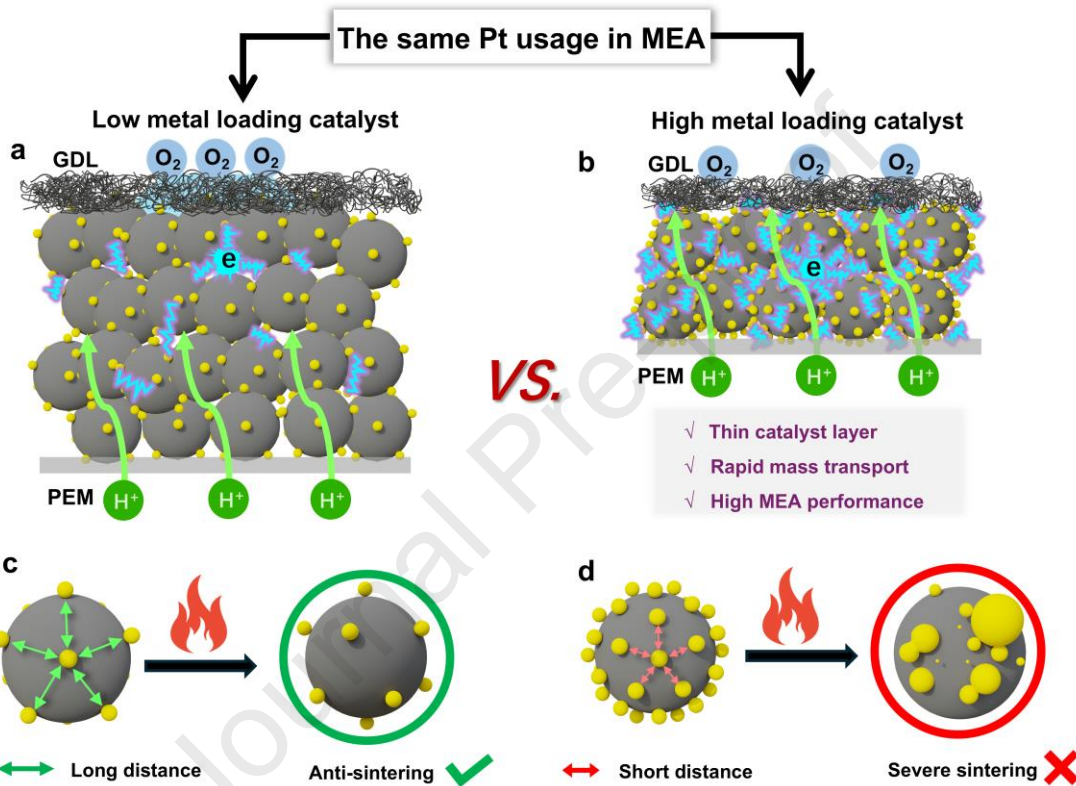
1 the ordering process [16–19], which inevitably results in the severe nanoparticles (NPs)
2 coalescence and hence the declined ORR activity.

3 To address the above issues, many efforts have been devoted to exploring the anti-
4 sintering strategies for the synthesis of small-sized and efficient Pt-IMC/C catalysts.
5 Support engineering [20–23], physical isolation effect [24–26] and corresponding their
6 derivative methods [27–29] are the typical and effective approaches to protect the NPs
7 against sintering under high temperature through inhibiting the migration and
8 coalescence of NPs respectively. Despite the great advances, the most studies always
9 focus on the Pt-IMC/C with the low metal loading [18,30–32], which is detrimental for
10 the performance transferring from ideal rotating disk electrode (RDE) to the practical
11 membrane electrode assembly (MEA). On the contrary, the catalyst with high metal
12 loading (i.e., high metal mass fraction within the catalyst) is the essential choice from
13 the vantage point of PEMFC industrial applications owing to its high electronic
14 conductivity, thin catalytic layer and rapid mass-transfer relative to the low metal
15 loading catalyst (Scheme a and b), facilitating the high-efficient performance
16 expression in MEA [33]. Unfortunately, there are few reports on the study of Pt-IMC/C
17 catalysts with high metal loading [34,35]. On the one hand, the academia is keen to
18 explore the low precious metal catalysts and pursue the reduction in precious metal
19 usage [36]. On the other hand, the NPs under high metal loading system may readily
20 encounter to each other and grow into the large NPs [37,38] (Scheme d) during the
21 high-temperature annealing, which increases the difficulty in the synthesis of small-size
22 Pt-IMC/C. Given the above considerations, the agglomeration of Pt-IMC/C with high
23 metal loading may not be effectively alleviated by the typical anti-sintering strategy
24 alone. As a matter of fact, the root of the NPs sintering is the thermal-treatment driven
25 particle migration and coalescence (PMC) or Ostwald ripening (OR) [39]. If the

1 ordering transformation temperature can be declined, the sintering of NPs would be
2 significantly inhibited. Of note that, according to the binary Pt-based phased-diagram
3 [40], the IMC structure is thermodynamically favorable under the low temperature in
4 comparison with their disordered alloys, which manifests that alloying process
5 dominates the IMC formation [14,17]. Recently, low-melting-point metal (LMPM)
6 doping strategy [15] has been reported to reduce the energy barrier of atomic diffusion
7 and improve the degree of ordering. Li [41] et al. can even reduce the ordering
8 transformation temperature to 450 °C by doping Sn and Ga metals. Nevertheless, the
9 standard electrode potential of LMPM is generally negative, which might increase the
10 risk of foreign metal leaching when working under PEMFC conditions. Thus, there
11 remains an urgent need to develop a facile yet large-scale preparation method to resolve
12 the sintering problem for the high-loaded Pt-IMC/C catalysts.

13 Herein, we present a concentration-gradient driven atom diffusion strategy to
14 promote the structural evolution from high-loaded Pt seed to L₁₀-type PtCo-IMC
15 structure. X-ray diffraction (XRD), X-ray adsorption spectroscopy (XAS), inductively
16 coupled plasma (ICP) measurements combined with molecular dynamic (MD)
17 simulations elucidate that locally concentrated Co atoms around Pt-seeds not only
18 accelerate the atom diffusion and promote the PtCo alloying under the relatively low
19 temperature, but also act as the protective isolator for the NPs against coalescence.
20 Temperature-dependent multiple characteristic techniques are further performed to
21 unveil the structural evolution mechanism upon heating process. As a result, the high-
22 loaded (44.3 wt.%) and small-sized (sub-5 nm) L₁₀-PtCo-IMC/C catalyst exhibits
23 desirable ORR activity (Mass activity (MA) = 0.57 A mg_(Pt)⁻¹ at 0.9 V vs. RHE)
24 together with the excellent durability. Encouragingly, membrane electrode assembly
25 (MEA) integrated with such catalyst at low cathodic Pt usage (0.10 mg cm⁻²) can

1 achieve a maximum power density of 1.15 W cm^{-2} and impressive stability under H_2 -
 2 air conditions. This methodology enables the preparation of 20 g-level catalysts in a
 3 single batch, demonstrating its potential for industrial application. Our findings provide
 4 insights into the efficient formation of intermetallic compounds, paving the way for
 5 their broader application in PEMFCs.



6
 7 **Scheme.** Comparisons of (a) low metal loading (b) and high metal loading catalyst in
 8 catalytic layer of MEA; sintering behaviors under high-temperature annealing for (c)
 9 low metal loading and (d) high metal loading catalysts.

10
 11 **2. Results and discussion**

12 **2.1. Concentration-gradient-driven atom diffusion and ordering**

13 Fig. 1 illustrates the synthesis schematic diagram of PtCo-IMC/C catalyst.
 14 Ultrasmall Pt seeds with an average size of approximately 2 nm (Fig. S1) are
 15 homogeneously dispersed on XC-72R (Pt-SD/C) with a metal loading of ca. 40 wt.%,

which is prepared by the decomposition of the Pt-carbonyl method as reported in our previous literature [35]. Cobalt chloride (CoCl_2) is appropriately wet-impregnated on Pt-SD/C and freeze-dried to form the precursor powder (Pt-SD/Co), which is subsequently annealed at specific temperature in a 10 vol% H_2/Ar atmosphere and acid-washed to obtain the target catalyst. During the synthesis, we found local Co concentration around Pt-SD are identified as a critical factor that influences the alloying and ordering processes. The local Co concentration gradients can be simply regulated through altering the feeding mole ratio of Co/Pt from 1:1 to 4:1. The higher Co/Pt ratio, the higher the concentration gradients.



XRD was first employed to explore the influence of Co concentration gradient on atom diffusion and PtCo alloying. It is observed that the Pt-SD/Co-X ($X = 1, 2, 3$ and 4) samples annealing at $400\text{ }^\circ\text{C}$ show the same phase structure (Fig. S2), demonstrating the feeding ratio of Co/Pt does not impact the alloying process under the relatively low temperature. Interestingly, when annealing at 500 and $600\text{ }^\circ\text{C}$ for 0.5 h (Figs. S3 and 2a), the degree of positive-shift for diffraction peaks gradually magnify as the increase in concentration gradients (i.e., feeding ratio of Co/Pt from 1 to 4), definitely assessing the strong dependence of PtCo alloying on the local Co concentration gradients (Fig.

1 S4). Notably, the Pt-SD/Co-1-600-0.5h sample shows the asymmetrical characteristic
2 peak compared to the other samples, indicative of the inhomogeneous phase structure.
3 Considering no obvious ordering transformation occur at 600 °C for 0.5h, the duration
4 time prolongs to 2h and the XRD patterns are illustrated in Fig. 2b. Except for Pt-
5 SD/Co-1, other samples almost accomplish the alloying process to form the Pt1Co1
6 alloy structure. Meanwhile, the superlattice peaks can be clearly observed for Pt-
7 SD/Co-2 and 3 samples while that for Pt-SD/Co-1 and 4 is illegible, implying that the
8 moderate Co concentration gradient is important for the ordering transition.

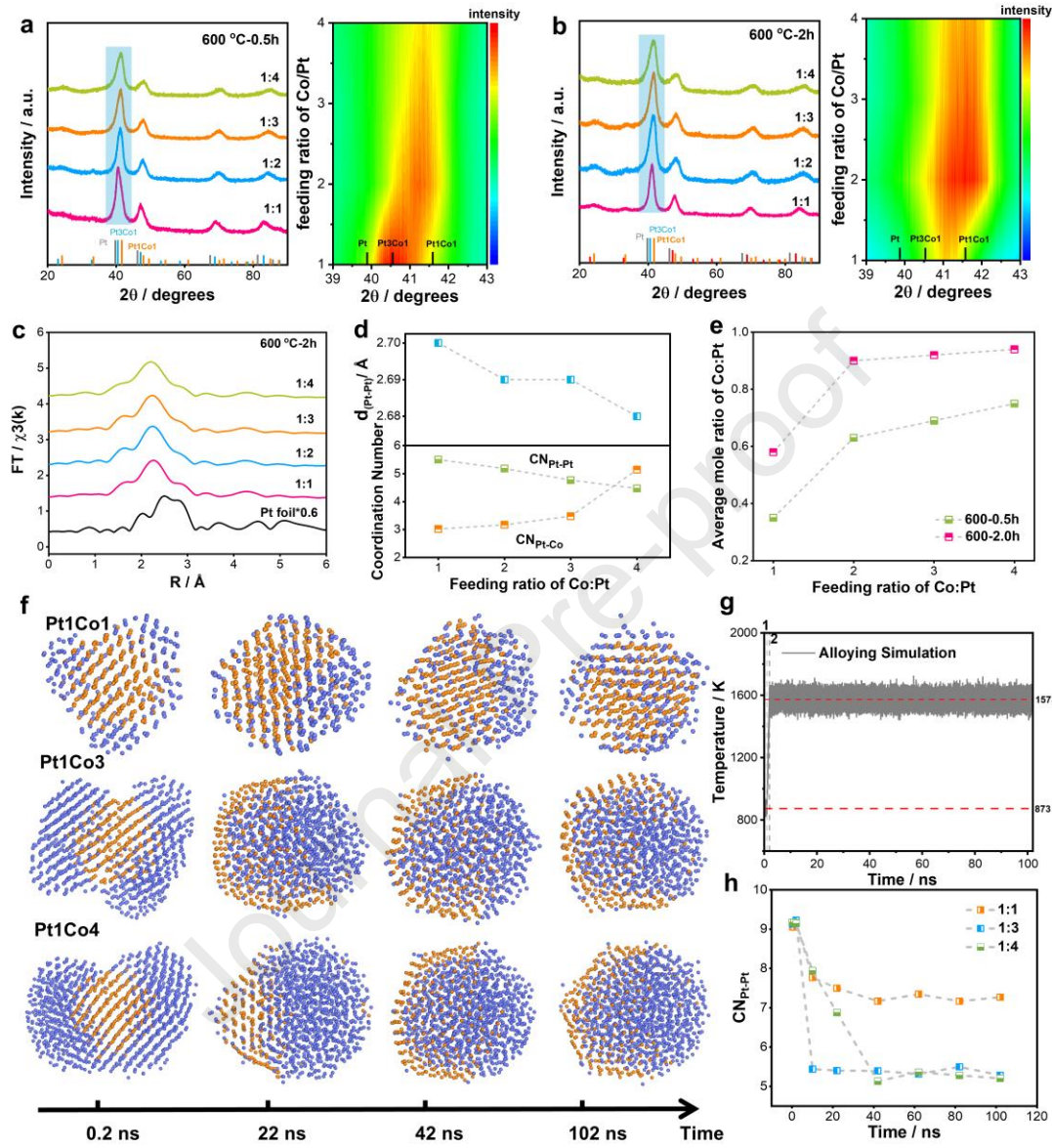
9 To further validate the promotion effect of Co concentration gradients on atom
10 diffusion process, extended X-ray adsorption fine structure (EXAFS) was also
11 performed. As shown in Fig. 2c, EXAFS spectra of Pt L₃-edge for Pt-SD/Co-X-600-2h
12 samples display that the Pt-Co scattering dominates for all the samples as comparison
13 with the Pt foil, indicative of the high alloy degrees after annealing at 600 °C for 2h. To
14 distinguish the difference in alloying degrees, the EXAFS spectra were fitted based on
15 the k-space data (Fig. S5). The fitting results (Fig. 2d) show that the distance of Pt–Pt
16 bond length ($d_{\text{Pt–Pt}}$) gradually decreases from 2.70 to 2.68 Å as the increase in Co
17 concentration gradients. Simultaneously, the average Pt–Pt coordination number ($\text{CN}_{\text{Pt–Pt}}$)
18 decreases from 5.50 to 4.47 while $\text{CN}_{\text{Pt–Co}}$ increases from 3.02 to 5.14. Above results
19 definitely verify that high Co concentration gradient is conducive to Co atom diffusion
20 and PtCo alloying, which is in accordance with aforementioned XRD results.

21 Inductively coupled plasma (ICP) was utilized to accurately analyze the regulation
22 of the atomic ratio of Pt and Co in the catalyst with the Co concentration gradient. As
23 shown in Fig. 2e, Table S1 and Table S2, the similar phenomenon is also observed for
24 the ICP results, which again reveals the increased average Co:Pt ratio within the PtCo
25 alloys as increasing the local Co concentration gradient under the same thermal-

1 treatment conditions. On basis of the above experiments, we speculate that the locally
2 high Co concentration gradients benefit to accelerate the diffusion of Co atom into Pt
3 lattice driven by concentration-gradient traction, thus enhancing the PtCo alloying
4 under relatively low temperature.

5 To further verify the facilitation effect of Co concentration-gradient on the alloying
6 of Pt-SD and Co precursor, molecular dynamics (MD) simulations were conducted
7 using the LAMMPS software package. Pt-SD with a diameter of approximately 2 nm
8 (273 atoms), representing a scale close to experimental conditions, were constructed as
9 shown in Fig. S6. Different numbers of Co shells were built around the Pt-SDs to obtain
10 Pt1Co1, Pt1Co3, and Pt1Co4 models (Fig. S7). After a certain period of equilibrium
11 simulations (Fig. S8), reasonable models were obtained as shown in the first column in
12 Fig. 1f. In the simulations of the alloying process of Pt and Co, the simulation
13 temperature was increased from 873 to 1573 K to accelerate the simulations, as shown
14 in Fig. 2g. The changes in the coordination number of Pt–Pt, denoted as CN_{Pt-Pt} , and
15 the atomic configurations over time during the simulation are presented in Fig. 2h. The
16 decrease in CN_{Pt-Pt} with time suggests that the Pt atoms in the Pt nanoparticles gradually
17 become more dispersed and eventually stabilize around a certain value. The stabilized
18 values of CN_{Pt-Pt} for both the Pt1Co3 and Pt1Co4 models are lower than that of the
19 Pt1Co1 model, and the Pt atoms in the Pt1Co3 and Pt1Co4 models, which were
20 originally inside the Co shells, tend to be dispersed on the surfaces of the Co
21 nanoparticles. This behavior may be attributed to the lower surface energy of Pt (1.48
22 J/m²) compared to that of Co (2.04 J/m²), inducing the formation of stable PtCo alloy
23 structure with Pt-enrich surface layer. This dynamic simulation also provides a
24 theoretical basis for the subsequent experimental synthesis of PtCo-IMC strucuture
25 with Pt-enriched surface layer. Above results indicate that the Pt atoms become more

1 dispersed and alloyed as the Co concentration increases, which thus facilitates the
 2 subsequent ordering process under the relatively low temperature.



3

4 **Fig. 2.** Mechanism of concentration-gradient driven alloying and ordering. XRD
 5 patterns of Pt-SD/Co-X annealed at 600 °C for (a) 0.5 h and (b) 2 h; (c) EXAFS spectra
 6 of Pt-SD/Co-X annealed at 600 °C for 2h and (d) corresponding the change tendency
 7 of Pt–Pt bond length and coordination number of Pt–Pt, Pt–Co as function of feeding
 8 ratio of Co/Pt; (e) Mole ratio of Co/Pt within the PtCo alloy annealing at 600 °C for
 9 0.5/2h as the function of feeding ratio of Co/Pt. (f) Snap shot images of structural
 10 evolution as a function of annealing time for the models of Pt-SD/Co-1, 3 and 4 and (g)
 11 simulation temperature during the alloying process (h) corresponding simulated
 12 coordination numbers of Pt–Pt.
 13

14 2.2. Concentrated Co combined with Pt-seeds enhance anti-sintering ability

1 In addition to promoting PtCo alloying, the locally concentrated Co also improves
2 the anti-sintering of NPs. As shown in Fig. S9, the calculated XRD average size
3 gradually decreases from 6.1 to 3.9 nm as the Co/Pt feeding ratio increases from 1 to 4,
4 which is attributed to the space-isolator effect of *in situ* formed Co nanoparticles. It is
5 noting that, the ordering degree of PtCo-IMC/C shows the volcano type trend dependent
6 on the Co concentration gradients (Fig. S10), and the Pt-SD/C-Co-3 achieves the
7 highest atomic order degree (~55%). A higher concentration gradient (Pt-SD/C-Co-4),
8 however, leads to a reduced ordering degree. We speculate the possible reason is that,
9 when annealing the Pt-SD/Co-X samples, only the Pt-SD/Co-4 can form the PtCo₃
10 phase because the excess Co precursor certainly generates Co nanoparticles around Pt
11 seeds. Accordingly, according to PtCo binary phase diagram, the phase transition
12 temperature (T_{PT}) of PtCo₃ is nearly 500 °C, much lower than that of Pt₁Co₁. The
13 temperature under T_{PT} is too low to overcome the kinetic energy barriers of atom
14 ordering, thus leading to the low ordering degree [40]. Moreover, when annealing the
15 Pt-SD/Co-3 sample at 700 °C for 2h, despite the intensive superlattice peaks located at
16 23.5° and 32.4°, corresponding to the (001) and (110) facets of L₁₀-Pt₁Co₁-IMC (Fig.
17 S9), the particle size is ca. 6 nm, larger than that of Pt-SD/Co-3-600 sample. In order
18 to balance the size and ordering degree, we finally optimize the Co/Pt feeding ratio of
19 3 and annealing temperature of 600 °C for 2h, respectively.

20 Except for the advantages of locally concentrated Co precursor in the formation of
21 small-sized PtCo-IMC/C nanoparticles, Pt-SD also plays a vital role in controlling NP
22 size. We employed two typical methods (direct annealing of Pt/Co salts and thermal-
23 treatment of PtCo alloy, see Experimental section) as comparison to prepare the PtCo
24 control samples under the same annealing conditions, denoted as PtCo/C-Salt and
25 PtCo/C-Alloy, respectively. XRD pattern (Fig. S11) of PtCo/C-Salt displays a mixed-

1 phase structure, including Pt₃Co and Pt₁Co₁, reflected by the obvious splitting of the
2 (111) characteristic peak. TEM images (Fig. S12) display a wide size distribution
3 ranging from a few to tens of nanometers. High-resolution TEM images further confirm
4 the coexistence of Pt and PtCo phases. This nonuniform size and phase structure are
5 probably attributed to unsynchronized reduction and random diffusion of Pt/Co atoms
6 in the salts. Fig. S13 displays the XRD patterns of the PtCo/C-Alloy sample before and
7 after thermal treatment. Although the homogeneous L₁₀-PtCo-IMC structure is well-
8 formed with apparent superlattice peaks and symmetrical characteristic peaks, the
9 average size dramatically increases from 3 to 8 nm after the thermal-treatment. TEM
10 and HR-TEM images (Fig. S14) also confirm that the average size of NPs is
11 approximately 8 nm. Such server sintering is attributed to thermal-coalescence under
12 high metal-loading and small surface area of carbon support. The above comparisons
13 undoubtedly confirm the advantage of Pt-SD in the synthesis of homogeneous and
14 small-sized PtCo-IMC/C catalyst.

15 To illustrate the universality of this concentration-gradient strategy to synthesize
16 small-sized PtM-IMCs/C catalysts, the ordered PtFe-IMC/C, PtZn-IMC/C and PtCu-
17 IMC/C were also prepared using the same method. As shown in Fig. S15, when
18 increasing the M/Pt feeding ratios, the sample exhibits higher alloying degree than that
19 of the counterpart prepared by the low M/Pt feeding ratio. It is noting that, the IMC
20 structure can be formed even under 350 °C for PtZn-IMC structure, again verifying that
21 locally high concentration-gradient can accelerate the atom-diffusion and realize the
22 ordering transformation under the relatively low temperature. Beyond that, the obtained
23 PtM-IMC show the desirable average size (< 6 nm). Interestingly, we found that the
24 ordering transition temperatures of these PtM-IMC (M = Fe, Co, Cu, Zn) are positively
25 correlated with the melting points of the transition metals (Fig. S16). This finding is
26 well consistent with the results recently reported in the literature [15,41], clarifying that
27 elements with low melting points have lower Pt–M bond strength, which in turn reduces

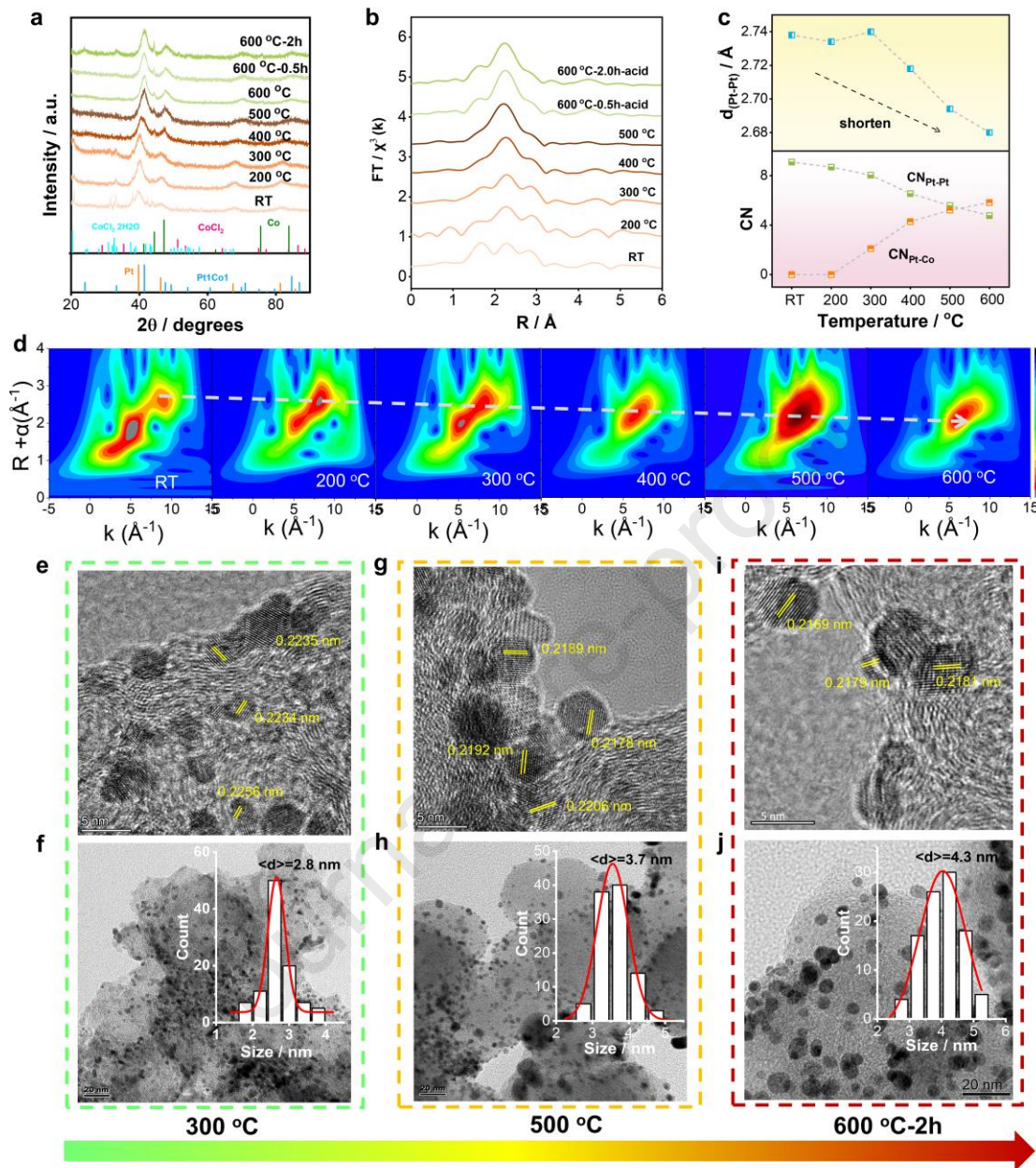
1 the atom diffusion activation barrier in PtM nanocrystal, thereby lowering the ordering
2 temperature.

3 Considering the simplicity of this method, we can realize the 20g/batch preparation
4 of PtCo-IMC/C catalyst (Fig. S17a) while ensuring the IMC structure and particle size
5 (Fig. S17b), manifesting the great potential of this method in mass production of low-
6 Pt catalysts. In addition, to validate the reproducibility and consistency of this method,
7 we prepared three batches of PtCo-IMC/C catalysts. The results of XRD, TEM (Figs.
8 S18, S19) and ICP (Table S3) all demonstrated that the method can achieve the batch
9 preparation of small-sized, high-loaded and ordered PtCo-IMC/C catalysts.

10 **2.3. Structural evolution monitoring**

11 To gain insight into the formation mechanism of sub-5 nm L₁₀-Pt1Co1-IMC/C,
12 structural evolution of Pt-SD/Co-3 during annealing was monitored by various
13 characterizations. Fig. 3a depicts the temperature-dependent XRD patterns. As the
14 temperature rises from room temperature (RT) to 500 °C, the characteristic diffraction
15 peaks gradually shift to high angle, indicating that the Co atoms constantly diffuse into
16 Pt lattice to induce the compression in c direction during the alloying process. Of
17 particularly note that the alloying transition occurs even under low temperature (e.g.,
18 200, 300 °C) when the Co ions cannot be reduced (pure CoCl₂/XC-72 mixture is
19 annealed under the same conditions, Fig. S20). This phenomenon implies that the Co
20 ions can be efficiently reduced to metallic Co atoms in the presence of ultrasmall Pt-
21 SDs even below 400 °C. In addition, the diffraction peaks stabilize at Pt1Co1 phase in
22 the range of 500–600 °C, manifesting the accomplishment of alloying process. The
23 superlattice peaks, corresponding to L₁₀ intermetallic structure, start to emerge at
24 600 °C and intensify after annealing for 2 h, reflecting the disorder-order transformation
25 process. Noteworthily, the Co salt and metallic Co phase exist at low (<400 °C) and
26 high (>400 °C) temperature stages, respectively, ensuring the anti-sintering of NPs

1 during the entire heating process (Fig. S21).



3 **Fig. 3.** Structural evolution from Pt seeds to L10-PtCo-IMC/C catalyst. Temperature-
4 dependence (a) XRD patterns (b) EXAFS for the Pt-SD/Co-3 sample (c) changes in Pt-
5 Pt bond length, Pt-Pt and Pt-Co coordination numbers (d) WT-XAS, (e, g, i) high-
6 resolution TEM images and (f, h, j) low-magnitude TEM images.

7

8 Temperature-dependent EXAFS and corresponding wavelet transformed XAS
9 were further conducted to investigate the local coordination environment evolution.
10 EXAFS (Figs. 3b and 3c) and fitting results (Fig. S22) demonstrate that $d_{\text{Pt-Pt}}$ gradually
11 shortens and reduces to $\sim 2.69 \text{ \AA}$ after annealing at 600 °C. Moreover, the $\text{CN}_{\text{Pt-Pt}}$ is

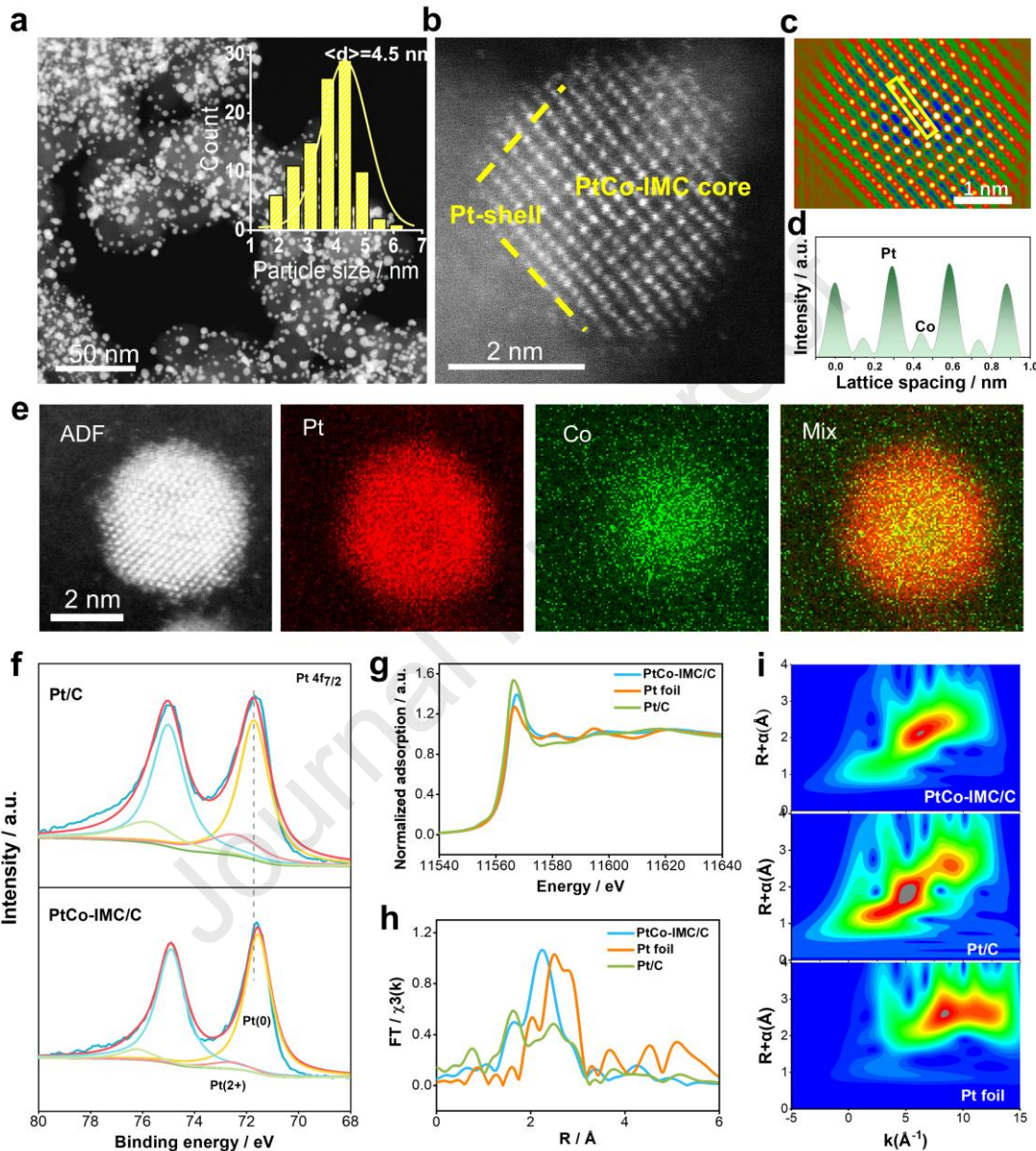
1 larger than CN_{Pt-Co} when heating below 600 °C, suggesting the existence of Pt-rich
2 ensembles in the disorder PtCo alloy. After annealing at 600 °C for 2h, the increased
3 CN_{Pt-Co} and decreased CN_{Pt-Pt} prove the atomic arrangement and ordering transition.
4 Beyond that, the temperature-dependent WT-XAS (Fig. 3d) displays that the WT
5 maximum shifts to low-k and low-R region with the increase of temperature, which is
6 ascribed to the transition from long Pt–Pt bond to short Pt–Co bond. Temperature-
7 dependent TEM was used to directly observe the morphology variations. HR-TEM
8 images of the sample annealing at 300 °C (Fig. 3e) show that the average lattice spacing
9 of most NPs is ca. 0.2244 ± 0.0012 nm, which is smaller than that of Pt(111) facet
10 (0.2265 nm) while larger than that of Pt₃Co(111) facet (0.2224 nm), signifying that the
11 slight Co atoms diffuse into Pt lattice, also evidenced by the EDS-mapping and line
12 profile (Fig. S23). Notably, the average size of NPs at this temperature is approximately
13 2.8 nm (Fig. 3f), slightly larger than the Pt-seed, demonstrating that the explosive
14 agglomeration does not happen at the initial heating stage. When elevating the
15 temperature to 500 °C, the size of NPs also shows a slight increase from 2.8 to 3.7 nm
16 (Fig. 3h). Importantly, the HR-TEM (Fig. 3g) presents the average lattice spacing of ca.
17 0.2191 ± 0.0013 nm, approaching to Pt₁Co₁(111) facet (0.2176 nm), implying the
18 alloying of large amount of Co atoms into Pt-SDs, which could also be proved by the
19 EDS line profile (Fig. S24). It is worth noting that several large Co nanoparticles can
20 be detected around alloy NPs (Fig. S25), which can be served as the isolators to protect
21 the alloy NPs against sintering. After annealing the sample at 600 °C for 2h, the Pt-SDs
22 show the average lattice spacing of ca. 0.2176 ± 0.005 nm and particle size of ca. 4.3
23 nm (Figs. 3i and 3j), which is ascribed to the formation of Pt₁Co₁ alloy phase, matching
24 well with the XRD and the EDS-mapping (Fig. S26) results. More significantly, the
25 superlattice reflection can be observed in the fast Fourier transform (FFT) pattern

1 derived from HR-TEM (Fig. S27), further confirming the disorder-order transition
2 occurs at this condition. By monitoring the structure evolution along the temperature,
3 we can better understand the formation mechanism of small-sized PtCo-IMC/C catalyst.

4 **2.4. Atomic and electronic structure investigation**

5 After the acid-washing treatment, the stable target catalyst is obtained. Unless
6 otherwise specified, the subsequent sample refers to Pt-SD/Co-3-600-2h, labeled as
7 PtCo-IMC/C. High-angle annular dark field scanning transition electron microscopy
8 (HAADF-STEM) was firstly used to study the morphology and atomic structure of the
9 optimized catalyst. Fig. 4a shows the representative low-magnification STEM images
10 of the as-prepared PtCo-IMC/C catalyst. The nanoparticles are uniformly distributed
11 over the carbon support with an average diameter of ca. 4.5 nm (Inset in Fig. 4a), which
12 is consistent with the XRD results, corroborating the successful synthesis of small-sized
13 nanoparticles. ICP measurements reveal that the metal loading of the obtained Pt₁Co₁-
14 IM/C is approximately 44.3 wt.% with a Pt/Co atom ratio of nearly 53:47. Atomic
15 number (Z)-contrast HAADF-STEM imaging was performed to analyze the atom
16 arrangement of PtCo-IMC NPs. A representative image (Fig. 4b) shows a core-shell
17 structure featured with an ordered IMC core covered by 2–3 layers thick Pt shell, which
18 can also be confirmed by EDS line profile (Fig. S28). The lattice spacing of 0.37 nm
19 corresponding to the superlattice of L₁₀-PtCo phase (001, PDF card, no. 43-1358) is
20 clearly observed, consistent well with the XRD result. The fake image of HAADF-
21 STEM (Fig. 4c) also clearly displays a layer-by-layer atom arrangement with periodic
22 brightness contrast, due to large difference in the Z-contrast of Pt and Co atom, in single
23 PtCo NP, indicative of the L₁₀-type face centered tetragonal (fct) intermetallic structure.
24 The line intensity profile along the yellow dashed rectangular area is shown in Fig. 3d.
25 It provides further evidence for the formation of the ordered intermetallic phase.

1 Moreover, EDS-mapping (Fig. 4e) shows the uniform distribution of Pt and Co element
 2 over the individual particle and the Co map is slightly smaller than the Pt map, again
 3 confirming the formation of core-shell structure.



4

5 **Fig. 4.** Characterizations of physical and electronic structures. (a) low magnitude
 6 STEM image and size distribution; (b) AC-STEM image of the single NP and (c)
 7 corresponding fake image and (d) line profile for the prepared PtCo-IMC/C catalyst;
 8 (e) EDS-mapping for the single PtCo-IMC NP; (f) XPS spectra for the PtCo-IMC/C and
 9 commercial Pt/C-JM catalysts; (g) XANES, (h) EXAFS and (i) WT-XAS spectra for
 10 the commercial Pt/C-JM, Pt foil and PtCo-IMC/C catalysts.
 11

12 Pt 4f XPS spectra of PtCo-IMC/C (Fig. 4f) show a negative shift of binding energy

1 compared to the commercial Pt/C one, demonstrating the alloying of Pt/Co atoms as
2 well as a down shift of d-band center. The Pt(II) percentage for PtCo-IMC/C is clearly
3 lower than that of Pt/C, implying the improvement in anti-oxidation and hence the
4 promoted ORR activity and durability. XANES at Pt L3-edge (Fig. 4g) shows that white
5 line area of L₁₀-PtCo-IMC/C is lower than that of Pt/C, but is similar to the Pt foil,
6 confirming that the metallic Pt with low valence state dominates in the L₁₀-PtCo-IMC/C
7 catalyst. Moreover, EXAFS (Fig. 4h) combined with fitting result display the
8 significantly shortened Pt–Pt bond (0.269 Å) as comparison with that of Pt/C (0.271 Å),
9 manifesting that the coordination of Co into Pt lattice induces the lattice contraction
10 and hence the favored ORR intrinsic activity. Of note that, the intensity of Pt–O
11 coordination path is much lower than that of Pt/C, attesting the improved oxidization
12 resistance for the ordered intermetallic structure, which is in line with the XPS and
13 XANES results. Besides, Wavelet transform (WT) of Pt L3-edge EXAFS oscillation
14 (Fig. 4i) displays that the intensity maximal of PtCo-IMC/C is centered at ~7.3 Å⁻¹,
15 lower than that of Pt foil (~8.1 Å⁻¹), which is associated with the Pt–Co attributions.
16 Moreover, comparing to the Pt/C and PtO₂ references, there is only one intensity
17 maximal and no Pt–O or Co–O attribution is observed, again confirming the oxygen-
18 resistance property for IMC structure.

19 **2.5. Electrochemical ORR evaluation**

20 Electrochemical ORR performance was evaluated by rotating disk electrode (RDE)
21 test in 0.1 M HClO₄ electrolyte. The commercial Pt/C (40 wt.%, John Mattery) and
22 PtCo/C-TKK (45 wt.%, Tanaka Kikinzoku Kogyo, Fig. S29) were also tested under the
23 same condition as comparisons. As shown in cyclic voltammetry (CV) curves (Fig.
24 S30a), the H under-potential deposition (UPD_H) areas for PtCo-IMC/C and PtCo/C-
25 TKK are apparently smaller than that of Pt/C-JM, implying that the particle growth

1 definitely leads to the decline of the electrochemical surface area (ECSA). The
2 calculated ECSAs for PtCo-IMC/C, Pt/C-JM and PtCo/C-TKK are 51.3, 78.5 and 41.6
3 m^2g^{-1} , respectively. Moreover, the PtCo catalysts show the positive shift of the potential
4 associated with oxidation of surface Pt (Pt-OH), which infers the weakened adsorption
5 energy of oxygen-species on Pt surface. Linear sweep voltammetry (LSV) on various
6 catalysts was further conducted to evaluate the catalytic activity.

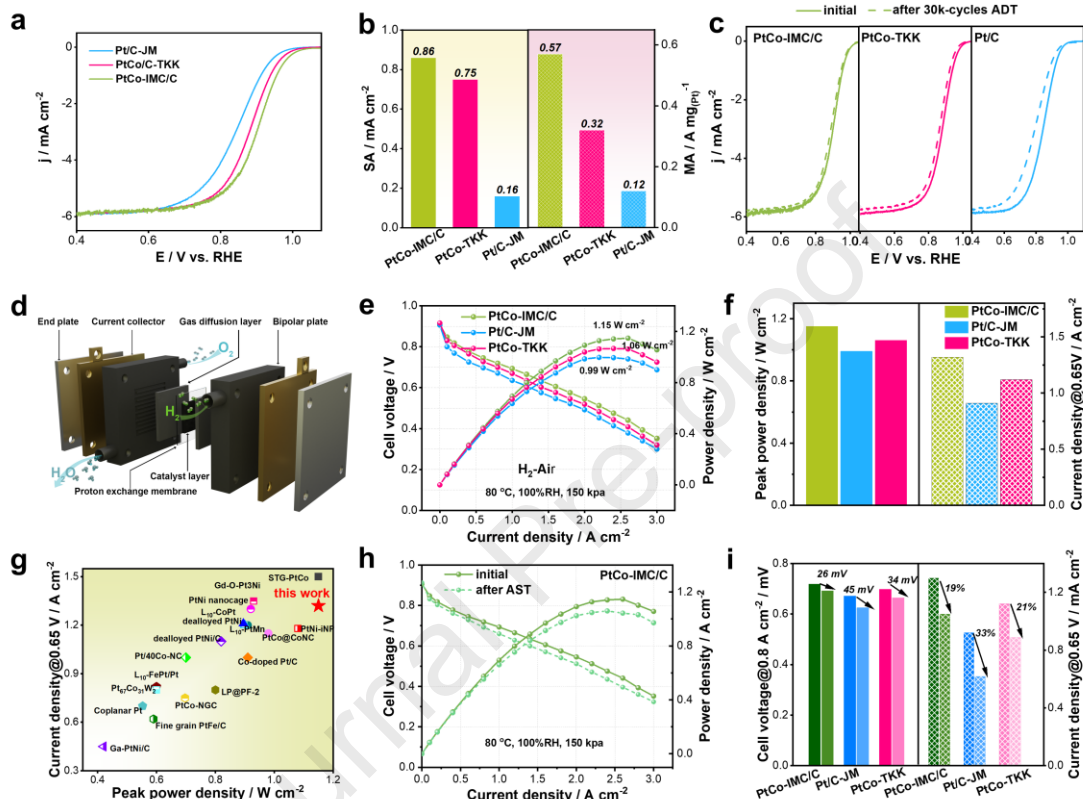
7 As shown in Fig. 5a, the ORR activity of PtCo-IMC/C is obviously higher than
8 those of Pt/C-JM and PtCo/C-TKK with the half-wave potential of 0.91, 0.89 and 0.85
9 V, respectively. The PtCo-IMC/C also delivers the superior specific activity (SA, 0.86
10 mA cm^{-2} , Fig. 5b) and mass activity (MA, $0.57 \text{ A mg}_{(\text{Pt})}^{-1}$), exceeding the PtCo/C-
11 TKK (0.75 mA cm^{-2} , $0.32 \text{ A mg}_{(\text{Pt})}^{-1}$) and Pt/C-JM (0.16 mA cm^{-2} , $0.12 \text{ A mg}_{(\text{Pt})}^{-1}$),
12 clarifying that the small-sized intermetallic catalyst greatly improves the intrinsic
13 activity and Pt utilization efficiency. Tafel plots (Fig. S30b) show that PtCo-IMC/C
14 exhibits the smallest Tafel slop (58.2 mV/dec) as comparison with those of PtCo/C-
15 TKK (59.6 mV/dec) and Pt/C-JM (63.1 mV/dec), indicative of the fast ORR kinetics.
16 Besides, the electrochemical impedance spectra (EIS, Fig. S31) and the fitting results
17 demonstrate that the charge-transfer impedance (Rct) shows a sharp decline compared
18 to the Pt/C-JM, also elucidating the dramatically promoted ORR intrinsic activity,
19 which is in good consistent with the Tafel results.

20 The durability was examined using accelerated durability test (ADT) by cycling
21 potentials from 0.6 to 1.0 V/RHE for 30k-cycles in O₂-saturated electrolyte. As shown
22 in Fig. 5c, the PtCo-IMC/C presents the encouraging durability with the acceptable
23 degradation, whereas the durability of Pt/C-JM and PtCo/C-TKK is much worse under
24 the same conditions. Concretely, the ECSA and MA of PtCo-IMC/C (Fig. S32) drop
25 only by 15.2/24.5%, while those of Pt/C and PtCo-TKK drop by 34.6/41.7% and

1 18.5/40.6%, respectively. The structural information of the catalyst after ADT were
2 analyzed by TEM and STEM to get insight into the degradation mechanism. As shown
3 in Fig. S33, PtCo-IMC/C displays a slight increase in average size from 4.5 to 5.6 nm.
4 In contrast, severe agglomeration of Pt nanoparticles can be observed on Pt/C-JM (Fig.
5 S34) catalyst and the size-distribution becomes broaden after ADT, owing to the
6 electrochemical Ostwald ripening process. It undoubtedly reveals the enhancement in
7 anti-oxidation of Pt atoms for the ordered IMC structure, which can inhibit the
8 dissolution of Pt and redeposition during high-potential cycling. Atomic STEM image
9 (Fig. S35a) shows that the ordered PtCo-IMC structure maintains with an alternative
10 arrangement of Pt and Co atoms. EDS-mapping (Fig. S35b) reveals the homogeneous
11 distribution of Pt and Co within the single nanoparticles, and the Co elemental map
12 becomes small, demonstrating the slight dissolution of outer Co atoms after ADT.

13 It is significantly crucial for practical application whether the catalytic activity of
14 catalyst can be efficiently expressed on MEA configuration or not. The optimized PtCo-
15 IMC/C was used as the cathodic catalyst for PEMFCs test (Fig. 5d). For comparison,
16 MEA with Pt/C-JM cathode was also examined under the same conditions. Fig. 5e
17 represents the steady-state polarization curves of MEA-PtCo-IMC/C, Pt/C-JM and
18 PtCo-TKK under the H₂-Air condition with the same cathodic Pt loading of 0.1 mg
19 cm⁻². Obviously, MEA-PtCo-IMC/C exhibits a superior discharging performance as
20 comparison to the MEA-Pt/C-JM and PtCo-TKK. Particularly, as shown in Fig. 5f, the
21 maximum power density (Pm) is 1.15 W cm⁻², which is higher than that of MEA-Pt/C-
22 JM (0.99 W cm⁻²) and MEA-PtCo-TKK (1.06 W cm⁻²). At an operating voltage of 0.65
23 V for practical fuel cell application, the MEA-PtCo-IMC/C delivers a current density
24 up to 1.32 A cm⁻², which exceeds that of Pt/C (0.91 A cm⁻²) and PtCo-TKK (1.12 A
25 cm⁻²) ones. It is noting that, when comparing the previously reported advanced Pt-

1 based electrocatalysts, although the intrinsic activity of the catalyst we prepared is at a
 2 medium level under RDE conditions, the MEA performance ranks at the forefront (Fig.
 3 4g and Table S4), again validating the superiority of high-loaded PtCo-IMC/C catalyst
 4 in the efficient performance expression in MEA.



5 **Fig. 5.** Evaluation of electrocatalytic performance in both RDE and MEA configurations. (a) LSV for the commercial Pt/C-JM, PtCo-TKK and PtCo-IMC/C samples; (b) The comparisons in SA and MA@0.9 V for various samples; (c) LSV curves before and after 30k-cycles ADT; (d) Illustration diagram of the single fuel cell setup; (e) Steady-state polarization curves of MEAs prepared by the commercial Pt/C-JM, PtCo-IMC/C and PtCo-TKK as cathode (anode: 0.05 mg_(Pt) cm⁻², cathode: 0.1 mg_(Pt) cm⁻²); (f) The comparison of peak power density and current density@0.65 V; (g) The comparison of performance with other reported advanced Pt-based ORR catalyst in H₂-air fuel cells; (h) MEA-PtCo-IMC/C before and after 30k-cycles AST; (i) Drops in cell voltage@0.8 A cm⁻² and current density@0.65 V after AST test.

17 CV was further performed on the MEAs, as shown in Fig. S36a. The ECSA in
 18 MEA configuration is calculated to 37.4 and 54.7 m²g⁻¹ for PtCo-IMC/C and Pt/C,
 19 respectively. The Pt utilization efficiency in MEAs were calculated by obtaining the
 20 values of the ECSA measured in the MEA to that measured in the RDE. The result (Fig.

S36b) shows that MEA-PtCo-IMC/C exhibits a similar utilization efficiency of Pt (73%) as comparison with that of MEA-Pt/C-JM (71%). EIS was further performed to investigate the impact of two electrocatalysts on the performance of MEAs. As shown in Fig. S37, with the increase in current density from 0.1 to 1.5 A cm⁻², the diameter of semicircle gradually decreases, indicative of the accelerated charge transfer rate. Of note, the Warburg impedance appears in the low-frequency region when the current density is higher than 1.0 A cm⁻², demonstrating the appearance of mass-transfer polarization. It is well known that the MEA performance under extremely low current density is dominated by the intrinsic activity of electrocatalyst. Fig. S38 depicts the Nyquist plots of MEA with two electrocatalysts under the current density of 0.1 A cm⁻². The fitted charge transfer resistance (Rct) is 5.7 mΩ, that is smaller than that of MEA-Pt/C (6.6 mΩ), attesting the improvement in ORR intrinsic activity for the PtCo-IMC/C catalyst. At the high current density (1.5 A cm⁻², Fig. S39), both Rct (19.1 mΩ) and Ws (9.9 mΩ) of the MEA-PtCo-IMC/C are smaller than those of MEA-Pt/C-JM with the values of 28.1 and 12.6 mΩ, respectively, implying the promoted charge and mass-transfer after the formation of ordered PtCo-IMC structure, which well explains the performance enhancement in MEA configuration. In addition, in H₂-O₂ fuel cell, the MEA with PtCo-IMC/C delivers 2.04 W cm⁻² (Fig. S40a) at the current density of 4.0 A cm⁻², which is higher than that of MEA-Pt/C (1.89 W cm⁻²). In particular, the MA for PtCo-IMC/C calculated from IR-corrected polarization curves (Figs. S40b,c) is much higher than that of Pt/C, further proving the promoted intrinsic activity for the ordered IMC structure.

Accelerated stress test (AST) from 0.60 to 0.95 V was conducted to evaluate the stability of MEAs. Fig. 5h and Figs. S41a,b present the polarization curves of MEA-PtCo-IMC/C, Pt/C and PtCo-TKK before and after AST, respectively. The MEA-PtCo-

1 IMC/C displays a slight performance degradation with ~26 mV decline in cell
2 voltage@0.8 A cm⁻² (Fig. 5i), which is lower than that of DOE target (<30 mV@0.8 A
3 cm⁻²). At a practical application voltage of 0.65 V, the MEA shows a ~19% decay in
4 current density. As a contrast, MEA-Pt/C and PtCo-TKK show 45/34 mV-loss in cell
5 voltage@0.8 A cm⁻² and 33%/21% decline in current density at 0.65 V, demonstrating
6 the inferior stability, which is also consistent with the ADT results on RDE
7 configuration. CV curves on MEAs (Fig. S42) demonstrate that the attenuation value
8 in ECSA of MEA-PtCo-IMC/C is obviously lower than that of MEA-Pt/C, indicative
9 of the severer Ostwald ripening for Pt/C catalyst under practical operation conditions.

10 **3. Conclusions**

11 In this work, we introduced a concentration-gradient-driven Pt-seed structural
12 evolution strategy for the controllable synthesis of sub-5 nm, high-loaded PtCo
13 intermetallic compound/carbon (PtCo-IMC/C) catalysts. Microstructural analyses,
14 supported by MD simulations, demonstrated that high Co concentration gradients not
15 only accelerate atom diffusion at solid interfaces but also act as isolators, protecting
16 nanoparticles from sintering. This dual role facilitates the formation of small-sized IMC
17 catalysts even under high metal loading conditions. Through various temperature-
18 dependent characterizations, we monitored changes in size, phase structure, and
19 coordination environment of the Pt-SD/Co-3 precursor during the heating process,
20 providing deeper insights into the structural evolution mechanism. Importantly, this
21 strategy is extendable to the synthesis of other PtM-IMC/C (M = Fe, Zn, Cu) catalysts,
22 effectively lowering the ordering temperature and demonstrating the universality of this
23 method. The resulting PtCo-IMC/C catalyst exhibited promising performance in H₂-air
24 fuel cells, achieving a maximum power density of 1.15 W cm⁻² at a low Pt usage of 0.1
25 mg cm⁻². This approach paves the way for the future development of high-loaded

1 electrocatalysts for fuel cells.

2 **4. Experimental section**

3 *4.1. Synthesis of high-loaded Pt-SD/C precursor*

4 Ultrafine Pt-seeds supported on XC-72R was fabricated by the low temperature
5 decomposition of Pt-carbonyl clusters that is formed in the presence of $\text{H}_2\text{PtCl}_6 \cdot 6\text{H}_2\text{O}$
6 (purchased from Sigma-Aldrich), NaOH and CH_3COONa (purchased from Sinopharm
7 Chemical Reagent Co., Ltd.) with the mole ratio of 1:4:8 in the methanol solution.
8 Carbon monoxide (CO) was continuously purged into the above solution, stirring at 55
9 °C for at least 12 h to form the emerald solution. Thereafter, Vulcan XC-72R powder
10 was quickly added into the above solution to control the Pt weight loading of 40 wt.%
11 and continuously stirring for 8 h. Then, the solvent was evaporated at 70 °C under N_2
12 purging and the obtained sample was slowly oxidized at 0 °C for 2 days. Subsequently,
13 the black precipitate was washed with DI-water for 5 times and dried in vacuum oven
14 to obtain the Pt-SD/C powder.

15 *4.2. Preparation of Pt-SD/Co precursor*

16 The prepared Pt-SD/C and the CoCl_2 (purchased from Sigma-Aldrich) were
17 dispersed into 100 mL DI-water with the feeding ratio of Co/Pt ranging from 1:1 to 4:1.
18 After the ultrasonic for 6 h, the mixture solution was quickly frozen under liquid
19 nitrogen bath and then transferred to freeze-dry machine for 48 h to finally obtain the
20 Pt-SD/Co-X ($X = 1, 2, 3, 4$) precursor.

21 *4.3. Preparation of PtCo-IMC/C catalyst*

22 The as-prepared Pt-SD/Co-X precursor was annealed at different temperatures for
23 several hours under 10% H_2 -90%Ar atmosphere with the heating rate of 5 °C min⁻¹.
24 After natural cooling down to room temperature (ensuring the same cooling time), the
25 obtained powder was washed in 0.1 M HClO_4 solution for 12 h at 60 °C to finally get

1 the target catalyst.

2 *4.4. Preparation of PtCo/C-Salt and PtCo/C-Alloy control samples*

3 PtCo/C-Salt: $\text{H}_2\text{PtCl}_6 \cdot 6\text{H}_2\text{O}$ and CoCl_2 precursors with Co/Pt mole ratio of 3:1 are
4 well dissolved in DI-water. Thereafter, Vulcan XC-72R powder was added into above
5 solution to control the Pt weight loading of 40 wt.% and continuously stirring for 8 h.
6 Then, the mixture solution was quickly frozen under liquid nitrogen bath and then
7 transferred to freeze-dry machine for 48 h to finally obtain the precursor. The as-
8 prepared mixture precursor was annealed at 600 °C for 2 h under 10% H_2 -90%Ar
9 atmosphere with the heating rate of 5 °C min⁻¹. After natural cooling down to room
10 temperature, the obtained powder was washed in 0.1 M HClO_4 solution for 12 h at 60
11 °C to finally get the PtCo/C-Salt catalyst.

12 PtCo/C-Alloy: CoCl_2 was added to a solution of Vulcan XC-72R in ethylene glycol
13 (EG) after sonication for 30 min with an argon sparge. Afterwards, weighed amounts
14 of $\text{H}_2\text{PtCl}_6 \cdot 6\text{H}_2\text{O}$ and CoCl_2 at a Pt/Co molar ratio of 1:1.1 were added to the suspension
15 and it was stirred for 2 h. 0.5 M NaOH in EG was added while stirring to adjust the pH
16 to 11.0. Above solution was subjected to microwave heating for 10 min in a microwave
17 oven operated at 180 °C. After microwave irradiation, the suspension was cooled to
18 room temperature and the solid product was washed with distilled water until it was
19 free of Cl^- . It was then dried in a vacuum oven at 40 °C for 10 h. The obtained PtCo
20 precursor was annealed at 600 °C for 2 h under 10% H_2 -90% Ar atmosphere with the
21 heating rate of 5 °C min⁻¹. After natural cooling down to room temperature, the obtained
22 powder was washed in 0.1 M HClO_4 solution for 12 h at 60 °C to finally get the PtCo/C-
23 Alloy catalyst.

24 *4.5. Electrochemical characterization*

25 Cyclic voltammetry (CV) and linear sweep voltammetry (LSV) were performed on

1 rotating disk electrode (RDE, 5 mm diameter), which was polished by various Al₂O₃
 2 powders and cleaned in H₂O/ethanol solution. Then 2 mg of the prepared catalyst was
 3 dispersed into solution that contains 975 μL of DI-water, 1000 μL of isopropanol and
 4 25 μL of Nafion (5 wt.%) to get the catalyst slurry with concentration of 1 μg/μL. The
 5 catalyst loading was controlled to 15 μg_(Pt) cm⁻² by drop 8.5 μL of above catalyst slurry
 6 on the glass electrode. Electrochemical tests were conducted on the CHI 730E equipped
 7 with a three-electrode system, using GC coated with catalyst as working electrode,
 8 carbon rode as counter electrode and Hg/Hg₂SO₄ as reference electrode. All the LSV
 9 tests were conducted in 0.1 M HClO₄ with a rotation speed of 1600 rpm at a scan rate
 10 of 10 mV s⁻¹. Accelerated durability test (ADT) was conducted by cycling the catalyst
 11 with the potentials range from 0.6 to 1.1 V at a scan rate of 100 mV s⁻¹ under continuous
 12 purging O₂ in electrolyte.

13 *4.6. Ordering and alloying degrees calculation*

14 The ordering degree was estimated by comparing the normalized intensity of the
 15 (110) peak to the sum of the intensities of the (111) and (200) peaks between the
 16 experimental XRD patterns and standard Powder Diffraction File cards of L₁₀-PtCo.
 17 The calculation formula is as follows:

$$18 \text{ Ordering degree (\%)} = \frac{S_{110}^{exp}}{S_{111+200}^{exp}} \left/ \frac{I_{110}^{PDF}}{I_{111+200}^{PDF}} \right. *100\% \quad (1)$$

19 S_{110}^{exp} , $S_{111+200}^{exp}$ are the integrated area under (110) peak and the sum of integrated
 20 area under (111) and (200) peak of the experimental XRD pattern, respectively. I_{110}^{PDF} ,
 21 $I_{111+200}^{PDF}$ are the intensity at (110) peak and the sum of the intensity at (111) and (200)
 22 peak of the Powder Diffraction File, respectively.

1 The alloying degree was estimated by comparing the 2θ difference between the
 2 experimental PtCo (111) peak and Pt (111) peak with 2θ difference between the
 3 standard Powder Diffraction File cards of L_{10} -PtCo (111) and Pt (111)

$$4 \quad \text{Alloying degree (\%)} = \frac{(2\theta_{PtCo}^{exp} - 2\theta_{Pt}^{PDF})}{(2\theta_{L10-PtCo}^{PDF} - 2\theta_{Pt}^{PDF})} * 100\% \quad (2)$$

5 $2\theta_{PtCo}^{exp}$ is the 2θ value under (111) peak for the experimental PtCo XRD pattern,
 6 $2\theta_{Pt}^{PDF}$, $2\theta_{L10-PtCo}^{PDF}$ are the 2θ values under (111) peak for the Powder Diffraction File
 7 of Pt and L_{10} -PtCo, respectively.

8 4.7. Membrane assembly electrode (MEA) preparation and single fuel cell testing

9 The MEAs with a $2.5 \times 2.5 \text{ cm}^2$ active area were fabricated by catalyst coating
 10 membrane (CCM) method. $15 \mu\text{m}$ Gore membrane was selected as the proton exchange
 11 membrane. The catalyst inks were prepared by dispersing 40 wt.% Pt/C (anode) and as-
 12 prepared PtCo-IMC/C (cathode) with 25 wt.% Nafion in isopropanol/H₂O solution
 13 under ultrasonic for 3 h. The Pt loading was controlled to 0.05 (anode) and 0.1 mgcm-
 14 2 (cathode). The performance of PEMFCs were estimated by testing the steady-state
 15 polarization curves on Arbin Fuel Cell Testing System (Arbin Instrument Inc., USA,
 16 data was recorded per 2 min). The flow rate of H₂ and O₂/Air is 1.0/0.4 slpm and the
 17 testing temperature was 80 °C with 100 RH%. The back-pressure was fixed at 150 kpa.
 18 The high-frequency resistance of MEA was recorded using battery resistance meter.

19 4.8. Theory/calculation

20 Molecular dynamics simulations were conducted using the LAMMPS software
 21 package. A time step of 2 fs and the NVT ensemble were employed in all MD
 22 simulations. The Nosé-Hoover thermostat was utilized to control the temperature. The
 23 second nearest-neighbor modified embedded-atom method (2NN-MEAM) interatomic
 24 potential for the Pt-Co binary system was used to describe the atomic interactions. Pt

1 nanoparticles with a diameter of approximately 2 nm (273 atoms), representing a scale
2 close to experimental conditions, were constructed (see Figure S6) using the WulffPack
3 Python package. Different numbers of Co shells were manually built around the Pt
4 nanoparticles to obtain Pt₁Co₁, Pt₁Co₃, and Pt₁Co₄ models, as shown in Fig. S7.
5 These models were placed in a cubic simulation box (80 Å × 80 Å × 80 Å), and 50 ps
6 of MD simulations were first performed at 298 K. Subsequently, the temperature of the
7 entire system was ramped up from 298 to 873 K within 1 ns (see Fig. S8) to obtain
8 reasonable models at the experimental temperature.

9 In the equilibrium simulations, the Co shells were found to shrink and cluster with
10 the Pt nanoparticles. Therefore, in the simulations exploring the alloying process of Pt
11 and Co, the previously obtained reasonable models were placed in a smaller cubic
12 simulation box with dimensions of (60 Å × 60 Å × 60 Å), and the simulation
13 temperature was increased from 873 to 1573 K.

14

15 **Author contributions**

16 Q.Q. Cheng and H. Yang proposed the concept. Q.Q. Cheng, T. Wang, Y.Y Pan, B.
17 Yang and Y.B. Chen performed the experiments and simulations. Q.Q. Cheng wrote the
18 manuscript. All authors participated in data analysis and manuscript discussion.

19 **Competing financial interests**

20 The authors declare no competing financial interests.

21

22 **Acknowledgments**

23 This work was supported by the National Natural Science Foundation of China
24 (22472193), Shanghai Rising-Star Program (24QA2710500, Shanghai Scientific and
25 Technological Committee), Shanghai Science and Technology Innovation Action Plan

1 (23ZR1471000, 22511102500), Key Research and Development Project of Guangdong
 2 Province (2023B0909060003) and the BL14W1 beamline at Shanghai Synchrotron
 3 Radiation Facility (SSRF).

4

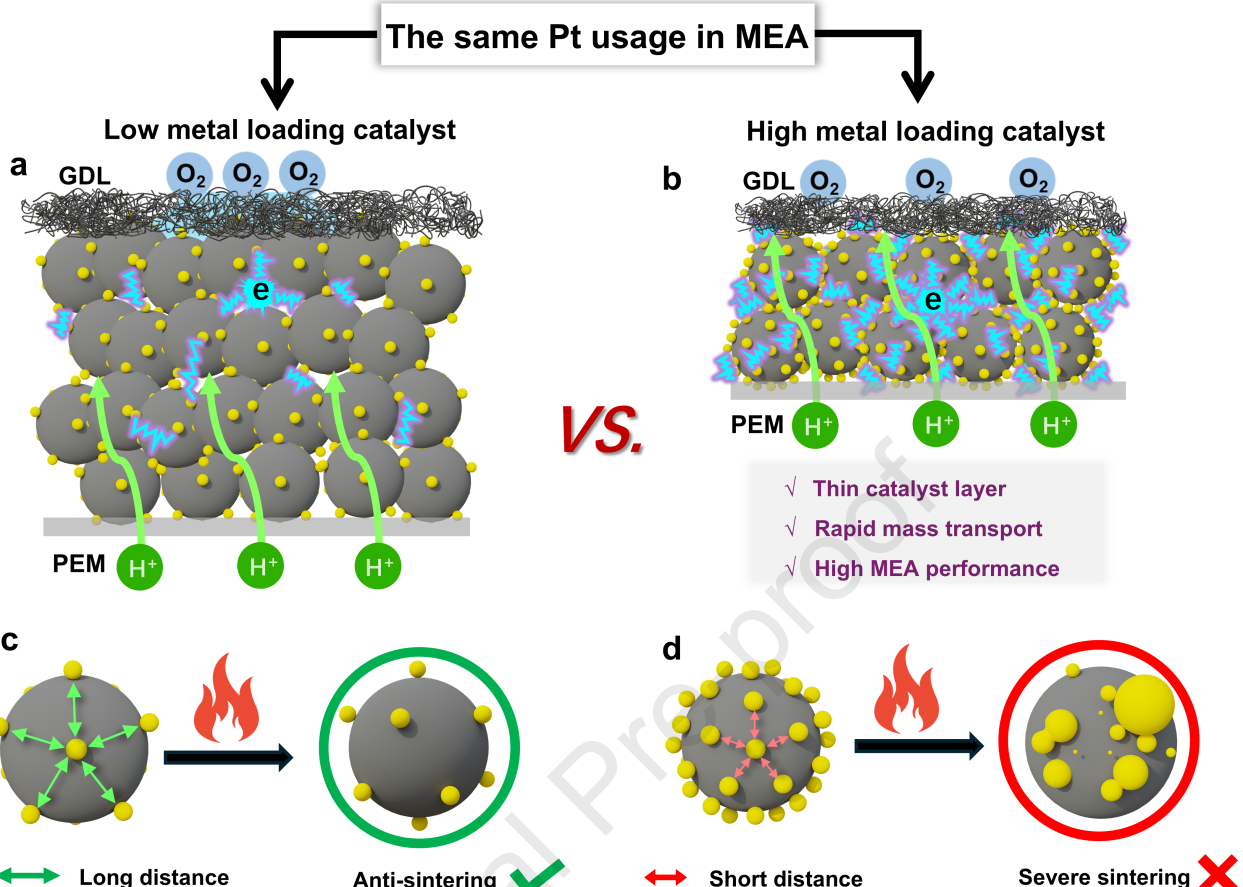
5 References

- 6 [1] Y.J. Wang, N. Zhao, B. Fang, H. Li, X.T. Bi, H. Wang, Carbon-supported Pt-based
 7 alloy electrocatalysts for the oxygen reduction reaction in polymer electrolyte
 8 membrane fuel cells: Particle size, shape, and composition manipulation and their
 9 impact to activity, *Chem. Rev.* 115 (2015) 3433–3467.
- 10 [2] M.K. Debe, Electrocatalyst approaches and challenges for automotive fuel cells,
 11 *Nature* 486 (2012) 43–51.
- 12 [3] L. Zheng, M. Niu, T. Zeng, X. Ge, Y. Wang, C. Guo, W. Yuan, D. Cao, L Zhang, C.
 13 Li, Assembling molybdenum-doped platinum clusters into a coral-like
 14 nanostructure for highly enhanced oxygen reduction, *eScience* 4 (2024) 100187–
 15 100195.
- 16 [4] X. Huang, Z. Zhao, L. Cao, Y. Chen, E. Zhu, Z. Lin, M. Li, A. Yan, A. Zettl, Y.M.
 17 Wang, High-performance transition metal-doped Pt₃Ni octahedra for oxygen
 18 reduction reaction, *Science* 348 (2015) 1230–1234.
- 19 [5] Y. Nie, L. Li, Z. Wei, Recent advancements in Pt and Pt-free catalysts for oxygen
 20 reduction reaction, *Chem. Soc. Rev.* 44 (2015) 2168–2201.
- 21 [6] M. Luo, S. Guo, Strain-controlled electrocatalysis on multimetallic nanomaterials,
 22 *Nat. Rev. Mater.* 2 (2017) 17059–17071.
- 23 [7] Y. Bing, H. Liu, L. Zhang, D. Ghosh, J. Zhang, Nanostructured Pt-alloy
 24 electrocatalysts for PEM fuel cell oxygen reduction reaction, *Chem. Soc. Rev.* 39
 25 (2010) 2184–2202.
- 26 [8] D. Wang, H.L. Xin, R. Hovden, H. Wang, Y. Yu, D.A. Muller, F.J. DiSalvo, H.D.
 27 Abruna, Structurally ordered intermetallic platinum-cobalt core-shell nanoparticles
 28 with enhanced activity and stability as oxygen reduction electrocatalysts, *Nat. Mater.*
 29 12 (2013) 81–87.
- 30 [9] W.P. Xiao, W. Lei, M.X. Gong, H.L. Xin, D.L. Wang, Recent advances of
 31 structurally ordered intermetallic nanoparticles for electrocatalysis, *ACS Catal.* 8
 32 (2018) 3237–3256.
- 33 [10] J. Greeley, I. Stephens, A. Bondarenko, T.P. Johansson, H.A. Hansen, T. Jaramillo,
 34 J. Rossmeisl, I. Chorkendorff, J.K. Nørskov, Alloys of platinum and early transition
 35 metals as oxygen reduction electrocatalysts, *Nat. Chem.* 1 (2009) 552–556.
- 36 [11] J. Lim, H. Shin, M. Kim, H. Lee, K.S. Lee, Y. Kwon, D. Song, S. Oh, H. Kim, E.
 37 Cho, Ga-doped Pt-Ni octahedral nanoparticles as a highly active and durable
 38 electrocatalyst for oxygen reduction reaction, *Nano Lett.* 18 (2018) 2450–2458.
- 39 [12] F. Lin, M. Li, L. Zeng, M. Luo, S. Guo, Intermetallic nanocrystals for fuel-cells-
 40 based electrocatalysis, *Chem. Rev.* 123 (2023) 12507–12593.
- 41 [13] J. Li, S. Sun, Intermetallic nanoparticles: Synthetic control and their enhanced
 42 electrocatalysis, *Acc. Chem. Res.* 52 (2019) 2015–2025.

- [14] J. Bai, L. Yang, Z. Jin, J. Ge, W. Xing, Advanced Pt-based intermetallic nanocrystals for the oxygen reduction reaction, *Chinese J. Catal.* 43 (2022) 1444–1458.
- [15] R.Y. Shao, X.C. Xu, Z.H. Zhou, W.J. Zeng, T.W. Song, P. Yin, A. Li, C.S. Ma, L. Tong, Y. Kong, H.W. Liang, Promoting ordering degree of intermetallic fuel cell catalysts by low-melting-point metal doping, *Nat. Commun.* 14 (2023) 5896.
- [16] Y. Yan, J.S. Du, K.D. Gilroy, D. Yang, Y. Xia, H. Zhang, Intermetallic nanocrystals: Syntheses and catalytic applications, *Adv. Mater.* 29 (2017) 1605997–1606026.
- [17] J. Liang, F. Ma, S. Hwang, X. Wang, J. Sokolowski, Q. Li, G. Wu, D. Su, Atomic arrangement engineering of metallic nanocrystals for energy-conversion electrocatalysis, *Joule* 3 (2019) 956–991.
- [18] J. Li, S. Sharma, X. Liu, Y.-T. Pan, J.S. Spendelow, M. Chi, Y. Jia, P. Zhang, D.A. Cullen, Z. Xi, H. Lin, Z. Yin, B. Shen, M. Muzzio, C. Yu, Y.S. Kim, A.A. Peterson, K.L. More, H. Zhu, S. Sun, Hard-magnet L_{10} -CoPt nanoparticles advance fuel cell catalysis, *Joule* 3 (2019) 124–135.
- [19] J. Wang, F. Pan, W. Chen, B. Li, D. Yang, P. Ming, X. Wei, C. Zhang, Pt-based intermetallic compound catalysts for the oxygen reduction reaction: Structural control at the atomic scale to achieve a win–win situation between catalytic activity and stability, *Electrochem. Energy Rev.* 6 (2023) 6.
- [20] X. Zeng, Y. Jing, S. Gao, W. Zhang, Y. Zhang, H. Liu, C. Liang, C. Ji, Y. Rao, J. Wu, B. Wang, Y. Yao, S. Yang, Hydrogenated borophene enabled synthesis of multielement intermetallic catalysts, *Nat. Commun.* 14 (2023) 7414–7424.
- [21] C.L. Yang, L.N. Wang, P. Yin, J. Liu, M.X. Chen, Q.Q. Yan, Z.S. Wang, S.L. Xu, S.Q. Chu, C. Cui, Sulfur-anchoring synthesis of platinum intermetallic nanoparticle catalysts for fuel cells, *Science* 374 (2021) 459–464.
- [22] X. Han, Q. Wang, Z. Zheng, Z. Nan, X. Zhang, Z. Song, M. Ma, J. Zheng, Q. Kuang, L. Zheng, Size-controlled intermetallic PtZn nanoparticles on n-doped carbon support for enhanced electrocatalytic oxygen reduction, *ACS Sustainable Chem. Eng.* 9 (2021) 3821–3827.
- [23] P. Yin, Q.Q. Yan, H.W. Liang, Strong metal-support interactions through sulfur-anchoring of metal catalysts on carbon supports, *Angew. Chem. Int. Ed.* 62 (2023) e202302819.
- [24] Q. Li, L. Wu, G. Wu, D. Su, H. Lv, S. Zhang, W. Zhu, A. Casimir, H. Zhu, A. Mendoza-Garcia, S. Sun, New approach to fully ordered fct-FePt nanoparticles for much enhanced electrocatalysis in acid, *Nano Lett.* 15 (2015) 2468–2473.
- [25] Z. Qi, C. Xiao, C. Liu, T.W. Goh, L. Zhou, R. Maligal-Ganesh, Y. Pei, X. Li, L.A. Curtiss, W. Huang, Sub-4 nm PtZn intermetallic nanoparticles for enhanced mass and specific activities in catalytic electrooxidation reaction, *J. Am. Chem. Soc.* 139 (2017) 4762–4768.
- [26] D.Y. Chung, S.W. Jun, G. Yoon, S.G. Kwon, D.Y. Shin, P. Seo, J.M. Yoo, H. Shin, Y.H. Chung, H. Kim, B.S. Mun, K.S. Lee, N.S. Lee, S.J. Yoo, D.H. Lim, K. Kang, Y.E. Sung, T. Hyeon, Highly durable and active PtFe nanocatalyst for electrochemical oxygen reduction reaction, *J. Am. Chem. Soc.* 137 (2015) 15478–15485.

- 1 [27] T.W. Song, C. Xu, Z.T. Sheng, H.K. Yan, L. Tong, J. Liu, W.J. Zeng, L.J. Zuo, P.
 2 Yin, M. Zuo, S.Q. Chu, P. Chen, H.W. Liang, Small molecule-assisted synthesis of
 3 carbon supported platinum intermetallic fuel cell catalysts, *Nat. Commun.* 13 (2022)
 4 6521.
- 5 [28] T.Y. Yoo, J.M. Yoo, A.K. Sinha, M.S. Bootharaju, E. Jung, H.S. Lee, B.H. Lee, J.
 6 Kim, W.H. Antink, Y.M. Kim, J. Lee, E. Lee, D.W. Lee, S.P. Cho, S.J. Yoo, Y.E.
 7 Sung, T. Hyeon, Direct synthesis of intermetallic platinum-alloy nanoparticles
 8 highly loaded on carbon supports for efficient electrocatalysis, *J. Am. Chem. Soc.*
 9 142 (2020) 14190–14200.
- 10 [29] Q. Gong, H. Zhang, H. Yu, S. Jeon, Y. Ren, Z. Yang, C.-J. Sun, E.A. Stach, A.C.
 11 Foucher, Y. Yu, M. Smart, G.M. Filippelli, D.A. Cullen, P. Liu, J. Xie, Amino-
 12 tethering synthesis strategy toward highly accessible sub-3-nm L_{10} -PtM catalysts
 13 for high-power fuel cells, *Matter* 6 (2023) 963–982.
- 14 [30] Y. Ma, A.N. Kuhn, W. Gao, T. Al-Zoubi, H. Du, X. Pan, H. Yang, Strong
 15 electrostatic adsorption approach to the synthesis of sub-three nanometer
 16 intermetallic platinum–cobalt oxygen reduction catalysts, *Nano Energy* 79 (2021)
 17 105465.
- 18 [31] X.X. Wang, S. Hwang, Y.T. Pan, K. Chen, Y. He, S. Karakalos, H. Zhang, J.S.
 19 Spendelow, D. Su, G. Wu, Ordered Pt₃Co intermetallic nanoparticles derived from
 20 metal-organic frameworks for oxygen reduction, *Nano Lett.* 18 (2018) 4163–4171.
- 21 [32] X. Liu, Y. Wang, J. Liang, S. Li, S. Zhang, D. Su, Z. Cai, Y. Huang, L. Elbaz, Q.
 22 Li, Introducing electron buffers into intermetallic pt alloys against surface
 23 polarization for high-performing fuel cells, *J. Am. Chem. Soc.* 146 (2024) 2033–
 24 2042.
- 25 [33] L. Shen, M. Ma, F. Tu, Z. Zhao, Y. Xia, K. Goh, L. Zhao, Z. Wang, G. Shao, Recent
 26 advances in high-loading catalysts for low-temperature fuel cells: From
 27 nanoparticle to single atom, *SusMat* 1 (2021) 569–592.
- 28 [34] Y. Wang, L. Zou, Q. Huang, Z. Zou, H. Yang, 3d carbon aerogel-supported PtNi
 29 intermetallic nanoparticles with high metal loading as a durable oxygen reduction
 30 electrocatalyst, *Int. J. Hydrogen Energy* 42 (2017) 26695–26703.
- 31 [35] Q. Cheng, S. Yang, C. Fu, L. Zou, Z. Jiang, J. Zhang, H. Yang, High-loaded
 32 sub-6 nm Pt₁Co₁ intermetallic compounds with highly efficient performance
 33 expression in PEMFCs, *Energy Environ. Sci.* 15 (2022) 278–286.
- 34 [36] L. Chong, J. Wen, J. Kubal, F.G. Sen, J. Zou, J. Greeley, M. Chan, H. Barkholtz,
 35 W. Ding, D.-J. Liu, Ultralow-loading platinum-cobalt fuel cell catalysts derived
 36 from imidazolate frameworks, *Science* 362 (2018) 1276–1281.
- 37 [37] P. Yin, S. Hu, K. Qian, Z. Wei, L.L. Zhang, Y. Lin, W. Huang, H. Xiong, W.X. Li,
 38 H.W. Liang, Quantification of critical particle distance for mitigating catalyst
 39 sintering, *Nat. Commun.* 12 (2021) 4865.
- 40 [38] T.-W. Song, L.-J. Zuo, M. Zuo, H.-W. Liang, Breaking trade-off between particle
 41 size and ordering degree of intermetallic catalysts for fuel cells, *J. Catal.* 419 (2023)
 42 19–25.
- 43 [39] T.W. Hansen, A.T. DeLaRiva, S.R. Challa, A.K. Datye, Sintering of catalytic
 44 nanoparticles: Particle migration or oswald ripening? *Acc. Chem. Res.* 46 (2013)

- 1 1720–1730.
- 2 [40] W.J. Zeng, C. Wang, Q.Q. Yan, P. Yin, L. Tong, H.W. Liang, Phase diagrams guide
3 synthesis of highly ordered intermetallic electrocatalysts: Separating alloying and
4 ordering stages, *Nat. Commun.* 13 (2022) 7654.
- 5 [41] J. Liang, Y. Wan, H. Lv, X. Liu, F. Lv, S. Li, J. Xu, Z. Deng, J. Liu, S. Zhang, Y.
6 Sun, M. Luo, G. Lu, J. Han, G. Wang, Y. Huang, S. Guo, Q. Li, Metal bond strength
7 regulation enables large-scale synthesis of intermetallic nanocrystals for practical
8 fuel cells, *Nat Mater* 23 (2024) 1259–1267.
- 9



1. Advanced microscopic and molecule-dynamics simulations reveal the promotion mechanism of concentration-gradient driven PtCo alloying and ordering
2. *Ex situ* XRD, XAS and TEM characterizations shed light on the structural evolution mechanism from Pt seeds to PtCo-IMC
3. High-loaded (44.3 wt.%) and small-sized (4.5 nm) PtCo-IMC/C is synthesized under relatively low temperature
4. PtCo-IMC/C catalyst achieves 1.15 W cm^{-2} under H₂-air fuel cell condition at a Pt loading of 0.1 mg cm^{-2}

Qingqing Cheng is an editorial board member for eScience and was not involved in the editorial review or the decision to publish this article. All authors declare that there are no competing interests.

